מכון ויצמן למדע
WEIZMANN INSTITUTE OF SCIENCE

Thesis for the degree
Master of Science

עבודת גמר (תזה) לתואר
מוסמך למדעים

Submitted to the Scientific Council of the
Weizmann Institute of Science
Rehovot, Israel

מוגשת למועצה המדעית של
מכון ויצמן למדע
רחובות, ישראל

By
Asad Awadallah

מאת
אסעד עוודאללה

אפיון צימוד ספין – מעוות בננו יהלומים
Characterization of spin-strain
coupling in nanodiamonds

Advisor:
Dr. Amit Finkler

מנחה:
ד"ר עמית פינקלר

November 2022

כסלו ה'תשפ"ג

Abstract

Color centers in nanodiamonds (fluorescent nanodiamonds) exhibit unique and interesting physical, chemical, and biological properties. These properties include, among others: robustness, inertness, photo-stability, and their controllable surface chemistry allowing different functional groups to be bonded to them. These properties and others make them a good candidate to be used as fluorescent dyes in bio-systems. One of the most famous color centers in nanodiamonds, the nitrogen-vacancy center, has a high magnetic field sensitivity, and nanoscale spatial resolution in ambient conditions, making it a spectacular, high precision nanosensor. However, nanodiamonds are indistinguishable from one another, and do not have a unique fingerprint. This makes it difficult to keep track of each single nanodiamond.

Here, we investigate and measure the possibility of adding another layer of information, which will potentially make each nanodiamond or cluster of nanodiamonds distinguishable. This information comes from lattice strain coupling to the nitrogen-vacancy electron spin properties, where an axial strain effectively modifies the zero field splitting, and the transverse strain lifts the degeneracy of the two degenerate states of the nitrogen-vacancy spin, resulting in a shift and a splitting of the optically detected magnetic resonances, respectively. These values have a distribution variance as we show, which gives uniqueness to each cluster of nanodiamonds, making them distinguishable from each other. This unique information about each cluster of fluorescent nanodiamonds, allows us potentially to track a specific nanodiamond in real time, such as in bio-markers. Moreover, we show their potential use as anti-counterfeiting labels, when dispersed on a small chip.

List of abbreviations

APD	Avalanche photodiode
APS	Ammonium persulfate
CVD	chemical vapor deposition
CW_ODMR	Continuous wave optically detected magnetic resonance
DI water	Deionized water
DND	Detonation nanodiamonds
DSB	Double side band
D_{gs}	$D_{groundstate}$
D_{es}	$D_{excitedstate}$
ESR	Electron spin resonance
FND	Fluorescent nanodiamonds
FWHM	Full width at half maximum
HPHT	High-pressure high temperature
IQ	In phase and quadrature phase
IPA	Isopropyl alcohol
ISC	Inter-system crossing
MW	Microwave
ND	Nanodiamonds
NV	Nitrogen vacancy center
ODMR	Optically detected magnetic resonance
OPX	Operator X
PCB	Printed circuit board
PL	Photoluminescence
PVD	Physical vapor deposition
SMF	Single mode fiber optic
SSB	Single side band
SW	Software
ZPL	Zero phonon line
ZFS	Zero field splitting

Contents

1 Introduction

Fluorescent nanodiamonds (FNDs) exhibit distinct properties, some inherited from diamond such as robustness, inertness, the non-toxic nature of diamond, and their diverse surface chemistry. Others are specific to the NV color center hosted in diamond lattice such as photostability, and absence of bleaching or blinking under high laser excitations. These properties make FNDs exploitable in various applications in a broad range of fields such as physics, biology, and chemistry. These applications include, among others, quantum sensing, and bio-labels.

Nitrogen vacancy (NV^-) centers are fluorescent lattice defects in diamond. Their delicate quantum nature allows them to be employed as sensors with high sensitivity and spatial resolution, to monitor external perturbations such as magnetic, electric, and strain fields. Their high stability and robustness, even on the nanometer scale, enable them to be employed as bio-markers. Another potentially important parameter of the diamond lattice is strain and its relation to the spin of the NV. In this study, we show that this strain can be exploited as another layer of information that can enhance previous applications such as alternatives to fluorescent dyes in biology, and open new fields of applications, such as anti-counterfeiting labels.

This strain makes FND clusters distinguishable from each other, which will potentially allow us to track a single particle, or a cluster of FNDs over a period of time, such as in bio-labels, replacing, for example, multi-color fluorescent dyes. Also, we show that a batch of FNDs dispersed on a glass substrate has a unique unclonable anti-counterfeiting strain distribution. This property makes them a good candidate for highly secure labels.

In this thesis I studied the strain distribution in clusters of nanodiamonds. Chapter two gives a brief introduction on diamond lattice, and NV centers, and then, discusses strain in general and lattice strain coupling to NV spin properties. Two more sections are in this chapter, the first explains ODMR technique, and the second gives a short summary of the various production methods of FNDs. The third chapter describes the methodology used, including all the setup, systems, and waveguides fabrication used in this study. The last section in this chapter discusses preparations and measurement plan followed in this study. Chapter four contains the measurements and results. Finally, chapter five gives a discussion and conclusion, showing potential applications of FNDs, and quantifying the distinguishability between two ODMR spectra of two different FNDs.

2 Scientific background

Diamond is an extraordinary material that exhibits a wide range of properties including chemical inertness [1], non-toxicity, and bio-compatibility [2], which make it an excellent material for labeling and sensing. It is a wide band-gap semiconductor (5.5 eV at room temperature), with a high refractive index of 2.4, and optical transparency from deep ultraviolet to the infrared. Moreover, it is an excellent thermal conductor ($2 \times 10^3\,\mathrm{W\,m^{-1}\,kg^{-1}}$) which is five times greater than copper [3]. The NV center is a point defect in the diamond crystal, consisting of a substitutional nitrogen atom adjacent to a vacant site having C_{3v} symmetry. It is a spin $S = 1$ system with a spin triplet in both ground and excited states and two intermediate singlets [4].

2.1 Diamond lattice structure

Diamond is an allotrope of carbon, having a diamond cubic structure named after it (Fig.1a). This structure is not one of the 14 Bravais lattices, but it can be thought of as two adjacent fcc cubic lattices displaced by $\frac{1}{4}$ of the diagonal along a cubic cell. The lattice parameter of diamond is $a = 3.567$ Å[5].

2.2 NV centers

The NV center is a point defect in a diamond lattice, created, for example, by irradiating the diamond lattice with nitrogen atoms using ion implantation, and after thermal treatment, a nitrogen-vacancy pair [7] will be created. Also, it can be found as-grown in the chemical vapor deposition process (CVD) [8]. Due to the diamond tetrahedral structure, four possible orientations of the NV center can be formed (Fig.2). There are two charge states of NV centers, negatively charged NV^-, and neutral NV^0, the different charge states can be identified by their zero phonon lines (ZPLs) occurring at 1.945 eV and 2.156 eV respectively. From here on we will consider the negatively charged NV center only.

The NV center has a triplet spin state in both the ground state and the excited state Fig.1b, the zero-field splitting of the ground state is $D_{gs} = 2.87$ GHz where the excited state has a zero-field splitting of $D_{es} = 1.42$ GHz. There is an intermediate system crossing state (ISC) with two singlets separated by an energy gap of 1042 nm, as we will see later, this state is very important for the optical detection of the spin state. The triplet spin state has one ground state $|0\rangle$, and two degenerate states $|\pm 1\rangle$, this degeneracy can be removed by applying a magnetic field $\mathbf{B}$ along the N-V axis, due to Zeeman effect and they split by $2\gamma\mathbf{B}$. Other fields can also cause this degeneracy to be removed, such as transverse strain, where some other fields can cause a shift of the degenerate state's center, affecting the zero-field splitting.

2.3 Strain

When materials are subject to force, they deform or strain. Stress is defined as the applied force per unit area, this force can be applied in three different ways, namely, tension, compression, and shear.

$$\sigma = \frac{F}{A_o} \tag{2.1}$$

Here, F is the force and A is the cross-sectional area, in SI units F (Newtons), A (m^2), and so stress will have units of ($\mathrm{N/m}^2$ = Pascal). Strain is defined as a unitless quantity referring

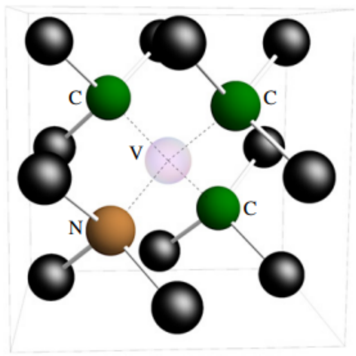

(a)

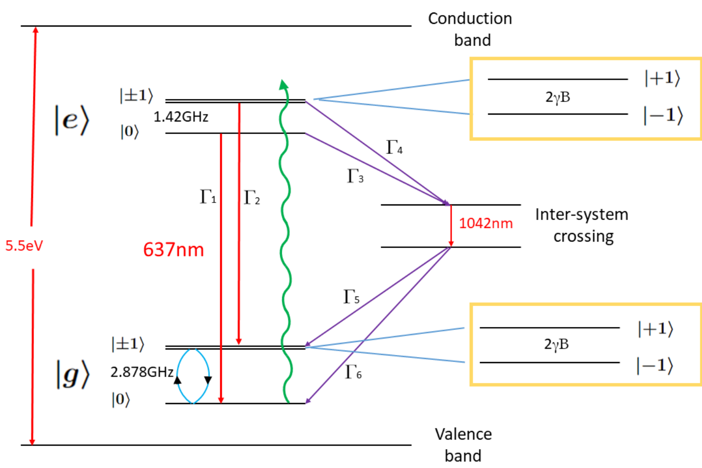

(b)

Figure 1: (a) Schematic of the nitrogen-vacancy center and diamond lattice depicting the vacancy (transparent), the nearest neighbor carbon atoms to the vacancy (green), the substitutional nitrogen atom (brown), and the next-to-nearest carbon neighbors to the vacancy (black)[6] (b) NV center energy diagram showing triplet spin state in both ground and excited states where two of them are degenerate, a bandgap of 5.5 eV is also shown. The zero-field splitting between $|0\rangle$ and $|\pm1\rangle$ in the ground state is $D_{gs} = 2.87$ GHz and in the excited state is $D_{es} = 1.42$ GHz. Upper and lower insets show the splitting of the degenerate states $|\pm1\rangle$ due to magnetic field B where γ is the gyromagnetic ratio.

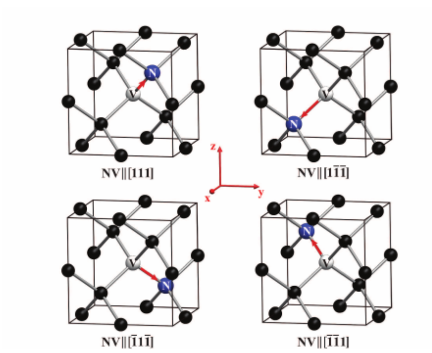

Figure 2: Each lattice shows one of four different NV orientations [9].

to the relative elongation to the original length when no stress is applied.

$$\epsilon = \frac{l - l_o}{l_o} = \frac{\Delta l}{l_o} \tag{2.2}$$

Two regimes rise depending on the magnitude of stress applied. The first regime is elastic deformation where the strain and stress are proportional to each other.

$$\sigma = E\epsilon \tag{2.3}$$

This is known as Hooke's law, where the constant of proportionality E (GPa) is called Young modulus. Elastic deformation is nonpermanent, which means that when the applied force is released the material returns to its original shape and length. The second regime is plastic deformation, which is permanent and non-reversible.

When a material is subject to a force, there will be a linear dependence between the strain and the stress up to some force, namely, the yield force, this is the elastic regime. Above the yield force plastic deformation will start to to occur. The residual strain in the fluorescent nanodiamonds is considered to be plastic deformation in the nanocrystals.

2.3.1 Effect of strain on NV spin properties

The ground state Hamiltonian for an NV, considering only the magnetic and strain fields for the purpose of this study is [10] [11],

$$H/h = D_0 S_z^2 + \gamma_{NV}\vec{S}\cdot\vec{B} + d_{\parallel}\epsilon_z S_z^2 - \frac{d_{\perp}}{2}[\epsilon_+ S_+^2 + \epsilon_- S_-^2] \tag{2.4}$$

where $D_0 = 2.87$ GHz is the zero-field splitting, $\gamma = 2.8$ MHz/G, $d_{\parallel}$ and $d_{\perp}$ are the parallel and transverse strain susceptibility parameters, $S_{\pm}$ are the spin raising and lowering operators, $\epsilon_{\parallel} = \epsilon_z$, $\epsilon_{\perp} = \sqrt{\epsilon_x^2 + \epsilon_y^2}$,$\tan(\phi_s) = \epsilon_y/\epsilon_x$ where $\epsilon_x, \epsilon_y, \epsilon_z$ are the diagonal components of the strain tensor defined in the NV basis.

Axial strain $\epsilon_{\parallel}$ results in shifting the zero-field splitting D_0, whereas a transverse strain results in mixing the degenerate states $|m_s = \pm 1\rangle$ and generating two non-degenerate states. We will denote the new mixed states $|\pm\rangle$ for more details see ref ([12]). The eigenvalues of the mixed states are,

$$f_{\pm} = D_0 + d_{\parallel} \in_{\parallel} \pm\sqrt{(\gamma B_z)^2 + (d_{\perp} \in_{\perp})^2}$$

Fig.3b shows an NV optically detected magnetic resonance spectra (ODMR) (see section 2.4) with no external fields (red), NV with axial strain (blue) shifted from the zero-field splitting, and with transverse strain (green) where we see a split in it.

Split and shift dependency on transverse and axial strain was investigated by J. Teissier et al. [11], using the cantilever experiment and modeled by Euler-Bernoulli theory [1]. They show a linear fit of this dependency Fig.3a. From the fitted data, they calculated $d_{\parallel} = 5.46 \pm 0.31$ GHz and $d_{\perp} = 19.63 \pm 0.40$ GHz.

2.4 Optically detected magnetic resonance (ODMR)

To exploit the NV center in different applications we need to be able to probe the spin state in a simple and efficient way. Several methods are used to do so, such as electron spin resonance (ESR), etc. Here we will use the optically detected magnetic resonance (ODMR) method.

ODMR is relatively a simple way to probe the spin transitions using spectroscopy, where in this method we exploit the differences in the radiative and the nonradiative transition rates and correlate them to spin transitions. For example, assuming that we have two states

[1] In this experiment a cantilever is fabricated with an NV center at its edge. A load is applied at the free edge, and using Euler-Bernoulli beam model, they calculate the equivalent strain on the NV center. Each time the load is changed the coupling of the strain to the NV spin properties is measured.

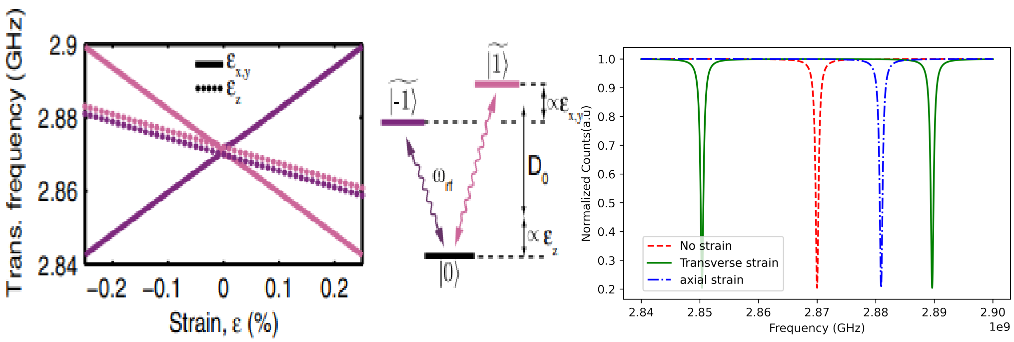

(a) **(b)**

Figure 3: (a) Results from J. Teissier et al. [11] show frequency shift and split caused by the cantilever bending (b) Results from J. Teissier et al. [11] showing frequency shifts and split vs. crystal strain. The effects of transverse strain ϵ_{xy} and axial strain ϵ_z are plotted separately (solid lines and dotted lines, respectively) (c) Calculation of an ODMR, showing no strain (red), axial strain (green), and transverse strain (blue) .

$|a\rangle$, and $|b\rangle$, state $|a\rangle$ decays mostly through a radiative path, where state $|b\rangle$, has another dominant path which is not radiative, assume 50:50 percent for the sake of the explanation. Now if all the spins are in state $|a\rangle$, the decay will go through the radiative path only, and we will have normalized photoluminescence (PL) equal to 100%. Now, if all the spins are in state $|b\rangle$, only 50% of them will decay through the radiative path, resulting in losing 50% of the photoluminescence (PL). In our case, the direct transitions between the excited state and the ground state are radiative whereas the transitions that go through the intersystem crossing (ISC) energy level are non-radiative [13].

In Fig.1b, Γ_1 and Γ_2 are radiative transitions, where Γ_{3-6} are non-radiative transitions. From the literature we see that $\Gamma_4 > \Gamma_3$ and $\Gamma_6 > \Gamma_5$ [13], here we assume that the degenerate states have equal rates. The first difference in the decaying rates from the excited states to the ISC will have an impact on the fluorescence intensity causing a drop of 30% in fluorescence at the resonance frequency (Fig. 4a), where the second rate difference will allow spin polarization. Consider the case where we excite electrons from the ground state to the first excited state using a laser pulse, electrons in the $|e, 0\rangle$ will decay to the $|g, 0\rangle$ in the radiative path due to selection rules, same for the other two degenerate states where they will also conserve their spin state, but in the case of the $|\pm 1\rangle$ another path will take place and become dominant which is the nonradiative path, the key point here is that it will preferentially decay to the $|0\rangle$ from the ISC ($\Gamma_6 > \Gamma_5$). Continuous application of laser will cause spin polarization of nearly 80% [14]. The other scenario that will cause a drop in fluorescence, which is the basis of ODMR, will be applying microwave radiation having a frequency equal to the spin resonance frequency in the ground state $D_{gs} = 2.87$ GHz, which will cause electrons to be excited to the $|\pm 1\rangle$ in the ground state. A laser pulse will excite electrons to the $|\pm 1\rangle$ in the first excited state, electrons in the $|\pm 1\rangle$ excited state will decay through the radiative path but also another dominant path will take place through the ISC. This path is nonradiative and so this will be reflected by a drop in the fluorescence by nearly 30% [15]. It is worth mentioning that if the two degenerate states are split due to a magnetic field (Fig. 4b), or any other field, then we will have two resonance frequencies $D_{gs} \pm \gamma B$ that will cause a drop in fluorescence, this splitting is the basis of magnetic field sensing, or more general field sensing that caused this splitting.

Two types of ODMR exist, continuous wave ODMR (CW-ODMR), and pulsed ODMR. In CW-ODMR the laser is continuously exciting the NV center (Fig. 4c), which is also continuously irradiated by microwave (MW). We sweep the MW over a range of frequencies

and fluorescence is recorded in each scanning frequency. The resonant frequency/frequencies are expected to be inside this scanning range and so when we scan over the resonant frequency we see a drop in the fluorescence as we mentioned above.
In pulsed ODMR the same technique is used (optical detection) as in CW-ODMR (Fig. 4c), but instead of applying continuous laser and MW, we first apply laser pulse to initialize the NV center, then we apply MW π pulse followed by a laser pulse to achieve both spin read out and polarization for next measurement. As in CW-ODMR if the MW frequency is equal to one of the resonant frequencies the spin state will be transferred to the degenerate state $|\pm 1\rangle$, which will, as we saw in CW-ODMR, reduce the fluorescence. Two benefits are achieved in pulsed-ODMR, the first is the reduction in linewidth (FWHM) caused by power broadening [16] leading to higher sensitivity. The second benefit becomes important in the case when we have two or more dips overlapping, making it hard to distinguish and characterize each dip. Thus reducing the linewidth will make these dips separable, making it possible to distinguish between them, and characterize them. Unlike CW-ODMR, pulsed-ODMR requires time-gated instrumentation for measurement.

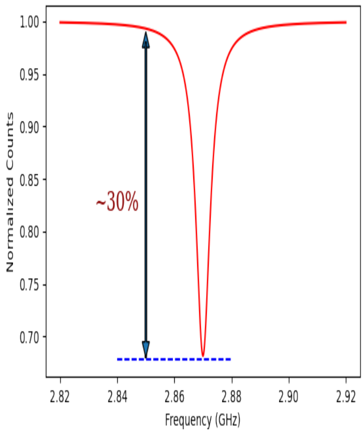

(a)

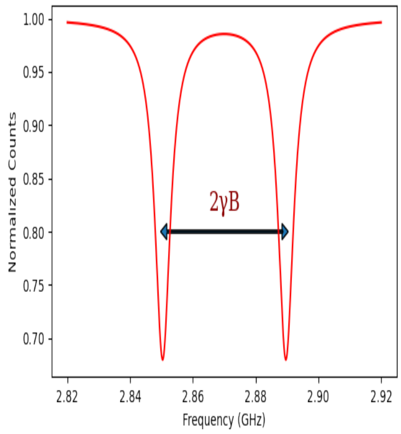

(b)

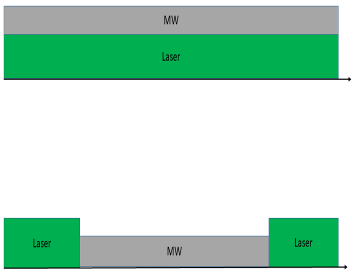

(c)

Figure 4: CW-ODMR and pulsed-ODMR. (a) ODMR measurement showing a drop of 30% in PL. (b) ODMR showing split of $2\gamma B$ caused by a magnetic field $\mathbf{B}$ aligned along the NV axis. (c) Sequence of ODMR measurements, the upper sequence is CW-ODMR, the lower sequence is pulsed ODMR.

2.5 Production of FNDs

Natural diamond has been known for a long time, and has been used as a gemstone and a cutting material due to its beauty, and hardness [17] respectively. In the last decades, FNDs gained more interest, due to their new applications in fields ranging from physics, chemistry, and biology. Since the first claim of synthesizing diamond from graphite in 1955 [18], several methods were developed. Here we will discuss some of the synthesis methods of FNDs.

NDs are categorized according to their size into three main groups, nanocrystalline particles ranging from tens of nanometers, ultrananocrystalline particles having a size of tens of nanometers, and diamondoids with a size of 1-2 nm.

The production of FNDs includes three main steps: synthesis, processing, and modification. This part will focus mainly on the synthesis. The processing step includes post synthesis treatment such as cleaning and impurities removal mainly caused by synthesis. The third step concerns the doping and surface functionalization of FNDs. Back to the first step, we will describe here four different methods of synthesis,

- Detonation [19]: Detonation nanodiamonds (DND) have a primary particle size of 4-5 nm, and are formed as the front detonation wave caused by the detonation of a powerful explosive mixture with low oxygen balance. The thermodynamic conditions for a stable diamond in the detonation process are about (25 GPa, 3000 K) and last about 1μs, followed by quick quenching in inert gaseous media, water, or ice. There are three main techniques of DND synthesis, according to the precursor used in detonation, the first is converting graphite to NDs at high pressure of 5 GPa in presence of a metal catalyst [20], the second method involves detonation of carbon precursors with other explosives in a closed chamber creating pressure (20-200 GPa) and temperature above 1727 °C, the third method involves using carbon containing explosives only.

- Ball milling of HPHT diamond: In HPHT process carbon containing precursors such as graphite, and Fe-Ni-C alloy, are used in conditions such as 5.5-8 GPa pressure, and 1000-1400 °C, conditions similar to 140-240 km deep in Earth. The size of these diamonds ranges from several tens to hundreds of microns. These particles are then converted to nano-size particles using ball milling techniques, such as nitrogen jet milling autogeneous micronization [21].

- Chemical vapor deposition (CVD): CVD diamonds have a wide range of grain sizes, morphologies, defect structures, and concentrations. Also, the properties may vary from nearly mono-crystalline to poly-crystalline grains. The precursors used in CVD nanodiamonds are mostly methane and hydrogen. To get a smaller size of CVD ND, argon is added to the mixture [22]. Several methods of CVD diamond exist, such as plasma-assisted CVD, thermally-assisted CVD, reactive vapor deposition, and a combination of these methods [23].

- Laser ablation [24]: A graphite is etched by a high-power pulsed laser in water at room temperature and normal pressure to produce nanocrystalline particles of diamonds. This method is good for laboratory-scale FND synthesis.

In this research, we worked with commercial FNDs, purchased from Adámas Nanotechnologies, Inc., which were prepared by ball milling of HPHT diamonds.

3 Methodology

3.1 Setup

The brain of this system is a device called OPX, manufactured by Quantum Machines. The OPX connects and controls all the other systems and sequence generation, through several analog and digital inputs and outputs, using an open source software called Qudi. As we saw in the previous sections we need an optical system to polarize and read-out the spin state. Also, a microwave system is necessary to manipulate the spin state. The OPX and the microwave system are connected together to perform fast frequency scans over a given frequency range. A piezoelectric stage is used to scan an $80 \times 80\,\mu m^2$ confocal image. One more important part is a permanent magnet controlled by three servo motors to move in the xyz direction. So generally we have five main parts:

1. Operator-X System (OPX).
2. Optical System (confocal microscope).
3. Microwave system.
4. Piezoelectric stage.
5. Permanent magnet connected to 3-axis moving servo motor.

3.1.1 Operator-X System (OPX)

OPX is the instrument that connects and controls all the other devices. It also allows for generating different pulse sequences through several analog and digital inputs and outputs. The software that is used in these experiments is Qudi [25], which is a software (SW) package that allows scanning, optimizing, sequence generation, fitting results, and many other functions.

3.1.2 Confocal microscope

ODMR measurement uses an optical system to initialize and read the spin state, a confocal microscope is used for this purpose. The main parts are shown in Fig. 6, where a green light laser diode (from Swabian instruments DLnsec) $\lambda = 520$ nm is used to generate the excitation pulse. The laser beam is guided through mirrors and lenses to a fiber coupler, then to a single mode fiber (SMF) to ensure a Gaussian profile of the beam. Again the beam is guided to a dichroic mirror through lenses and mirrors. The dichroic mirror is used to separate the excitation and emission beams, where it acts as a long pass filter allowing the laser beam to be transmitted and reflecting the emitted beam from the NV. Fig. 5 shows the transmission curve of the dichroic mirror. $\lambda = 576$ nm is the cut-off frequency where above this wavelength beam will be reflected. The laser beam ($\lambda = 520$) nm will pass through the dichroic mirror and then will be reflected through two mirrors to reach the objective (Olympus MPLFLN 100x, NA = 0.9), and focused on the sample. The photoluminescence (PL) from the NV center goes back through the same objective and reflected through the same mirrors tracing the incoming beam back to the dichroic mirror, but as we see in the transmission curve of the dichroic mirror, the beam will be reflected and not transmitted. The dichroic mirror will reflect it to two other mirrors and lenses to reach a 50 μm pinhole, which is regarded as the heart of the confocal microscope. The pinhole blocks out-of-focus light. Beams coming out from the pinhole will be split equally through a 50:50 beam splitter to two avalanche photodiodes (APD). The APD is a highly sensitive photon detector that can detect as low as one photon. In most of the experiments one APD should be enough, whereas some experiments such as auto-correlation use both detectors.

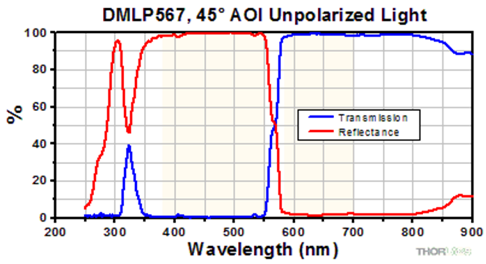

Figure 5: Transmission curve of dichroic mirror [26].

3.1.3 Microwave system

To manipulate electron spin states in NV^- centers, as we saw in ODMR, we need to scan over a spectrum of wavelengths in the microwave regime. For this purpose, I used a custom-built microwave scanning system (Fig. 8a).

The system consists of a microwave generator (SynthNV Pro from Windfreak Technologies, LLC), generating the center frequency, which I will name it here as f_{LO} (LO for the local oscillator). The output of the generator goes to an IQ mixer (Fig. 8b) where the other two inputs of the IQ mixer come from the OPX. This will generate the required scanning signal which will be then fed to the amplifier to achieve the needed power. A circulator will be added after the amplifier to prevent reflection. In general, we can use the generator only to scan over the required bandwidth, but the scanning will be slow, so we will use the OPX combined with the IQ mixer to scan over the required bandwidth. The IQ mixer needs to be fed with two signals having the same frequency and $\pm\frac{\pi}{2}$ phase shift. The $-\frac{\pi}{2}$ will allow scanning frequencies lower than the oscillator frequency and the $+\frac{\pi}{2}$ will scan frequencies higher than the oscillator frequency.

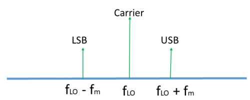

Figure 7: DSB with carrier spectrum. The three components are shown, LSB carrier, and USB.

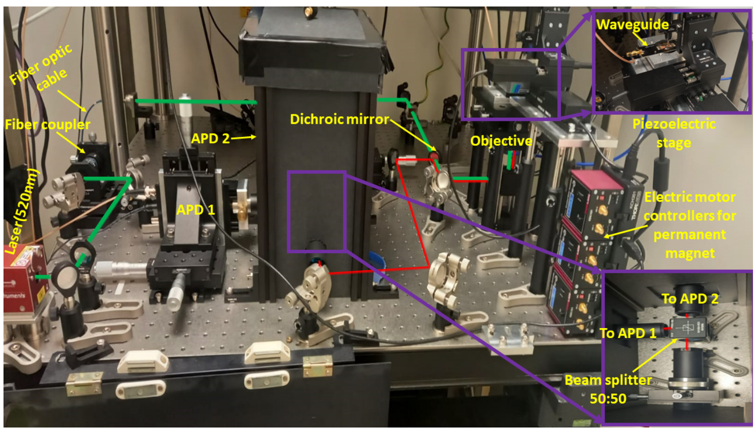

Figure 6: Photo of the custom-built confocal microscope.

The basic idea of this scanning microwave system comes from heterodyning, an idea that was first introduced by the Canadian inventor Reginald Fessenden. In heterodyning, two signals are introduced to the mixer to get the one heterodyned signal. In the most general case, we will get three components $f_{LO}-f$,$f_{LO}+f$ and the carrier frequency f_{LO} this situation is called double sideband (DSB) carrier included (local oscillator frequency, Fig. 7). Other cases are possible, for example, both sidebands exist but no carrier (DSB suppressed carrier), or only with a single sideband and carrier (SSB), or as in our case as we will see later, a single sideband with no carrier (SSB suppressed carrier), for a detailed mathematical investigation, see Appendix 6.1

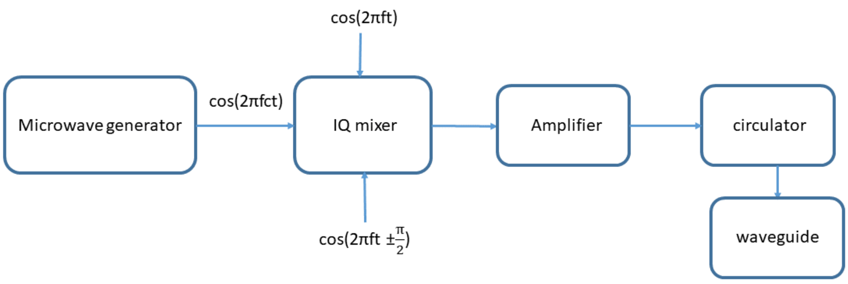

(a)

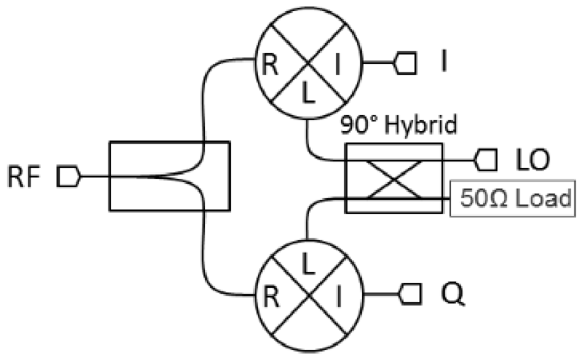

(b)

Figure 8: Microwave System. a) Block diagram of the microwave system. b) IQ mixer schematic diagram.

3.2 Waveguide

A very important part of this experiment is delivering electromagnetic waves in the microwave regime to the sample. A microwave waveguide was fabricated for this purpose. The waveguide should be compatible with the system, where it can be inserted in the confocal microscope and connected to the microwave generation system (Fig.12a). Also, we need to be able to disperse NDs on the waveguide in a way that we are still able to scan them in the confocal microscope. Both criteria were met by fabricating the waveguide on a 20 × 20 mm^2 glass substrate that will be connected to a custom-made PCB and easily connected to the system. Glass is transparent to visible light, which allows us to scan using the confocal microscope.

3.2.1 Waveguide fabrication

The fabrication of planar waveguides implies nanofabrication techniques and goes through four main processes, which are deposition, lithography, electroplating, and etching, Fig.9 shows the end rsult of the waveguide fabrication.

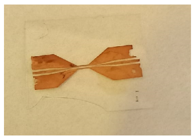

Figure 9: Copper co-planar waveguide fabricated on a glass substrate.

The fabrication method starts by depositing a 5 nm chromium adhesion layer, followed by a 300 nm copper layer. Using lithography we specify the area where we want to grow more copper and expose it, where the rest of the area will be covered by photoresist. A thicker layer of copper will be then grown using electroplating. Finally, we etch the undesired copper and chromium to get the final shape of the waveguide.
We fabricated the waveguide on 20×20 mm^2 and 160 µm thick glass substrates, so we start by:

1. Cleaning: we sonicate the substrates in acetone for five minutes, followed immediately by sonication in IPA for the same amount of time. Then dry each substrate with nitrogen gas.

2. Deposition: using physical vapor deposition (PVD), more specifically evaporation PVD, we deposit a copper layer and a chromium layer as seen in Fig.12b. The samples are placed on a sample holder, where each is attached using Kapton tape. The deposition will occur in a vacuum chamber where the sample holder is positioned in the upper part of the chamber upside down, and both metals are placed in crucibles beneath the holder. The metals are heated by electric current till they start to evaporate, and a layer of metal starts to grow. When the desired thickness of chromium is achieved we immediately start the copper evaporation as before.

3. Lithography: in the previous step we grew a copper seed layer. This layer has neither the right thickness nor the desired waveguide shape, where we need it to act as starting point for electroplating (seed layer). To perform electroplating to get the desired thickness and have the right waveguide shape at same time, we must expose only the relevant part which is the part that resembles the waveguide shape, and hide the rest. Using lithography we specify the region defining the waveguide shape and pattern it using positive mask, which means that only the waveguide shape will be exposed to electroplating and covering the rest with photoresist (Fig.12c).

   (a) Preparation: we rinse the samples in acetone, then IPA and dry with nitrogen gas.

   (b) Photoresist coating: we spin coat positive photoresist (AZ 4562) on the substrate to get the desired thickness of the resist, leave in ambient conditions for 15 minutes, then bake for 3 minutes on 100 °C plate.

   (c) Expose: using a mask aligner and a positive reticle, we expose the samples to UV light, the resist lying on the part making the shape of the waveguide then will be removed in the next step.

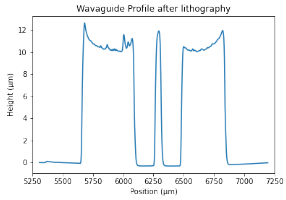

Figure 10: Waveguide profile showing photoresist thickness

(d) Develop: in this process, we want to remove the part of the resist that was not exposed to UV. We immerse the samples in a diluted developer (AZ351B) 1:3 in DI water, till we see that the resist layer upon the waveguide shape is completely removed. We can verify this, if not possible by eye, using a microscope, on average it takes 3 minutes. By this, the lithography process is completed and ready for the next step, Fig. 10 shows the shape and thickness of the photoresist after develop.

4. Electroplating: In lithography, we exposed the area resembling the waveguide shape to grow a thicker copper layer, and covered the rest, we will do this by electroplating (Fig.12d).
Electroplating is an electrochemical process where the copper cations are reduced at the cathode to the zero valence state, Fig.11a shows the setup we used to perform electroplating. To achieve the desired thickness two parameters are controlled, electric current and process time, equation 3.1 gives this relation while h (µm), I (mA/cm^2), and t (minutes). Appendix 6.2 shows a detailed derivation of this equation,

$$\frac{t_{total}}{h(\mu\text{m})} = \frac{45.16}{J} \tag{3.1}$$

We connect the sample to a bigger glass substrate covered by copper tape and adhere the sample from the sides with copper tape to the substrate. When the sample is placed in the electrolyte, the liquid will penetrate between the copper tape and the sample also between the copper tape and the substrate, this will prevent the current from flowing to the copper on the sample. To overcome this we add silver paste between the sample copper layer and the copper tape also between the copper tape and the substrate, which will ensure electrical conductive path to the copper seed layer, Fig.11b emphasize the silver paste connections.

5. Etching: we start by removing the resist by putting the samples in acetone for five minutes (Fig.12e, then we etch the copper by putting the samples in 8% APS solution till we start seeing the the copper layer disappearing (Fig.12f). To remove the chromium we put the samples in 32% HCl solution (Fig.12g).

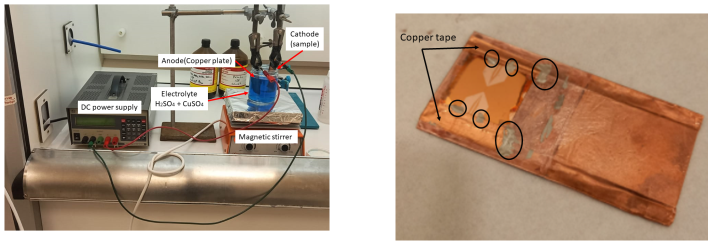

(a) (b)

Figure 11: (a) Copper electroplating Setup (b) Waveguide attached to a glass substrate covered with copper tape using copper tape, the circles show were the silver paste will be added.

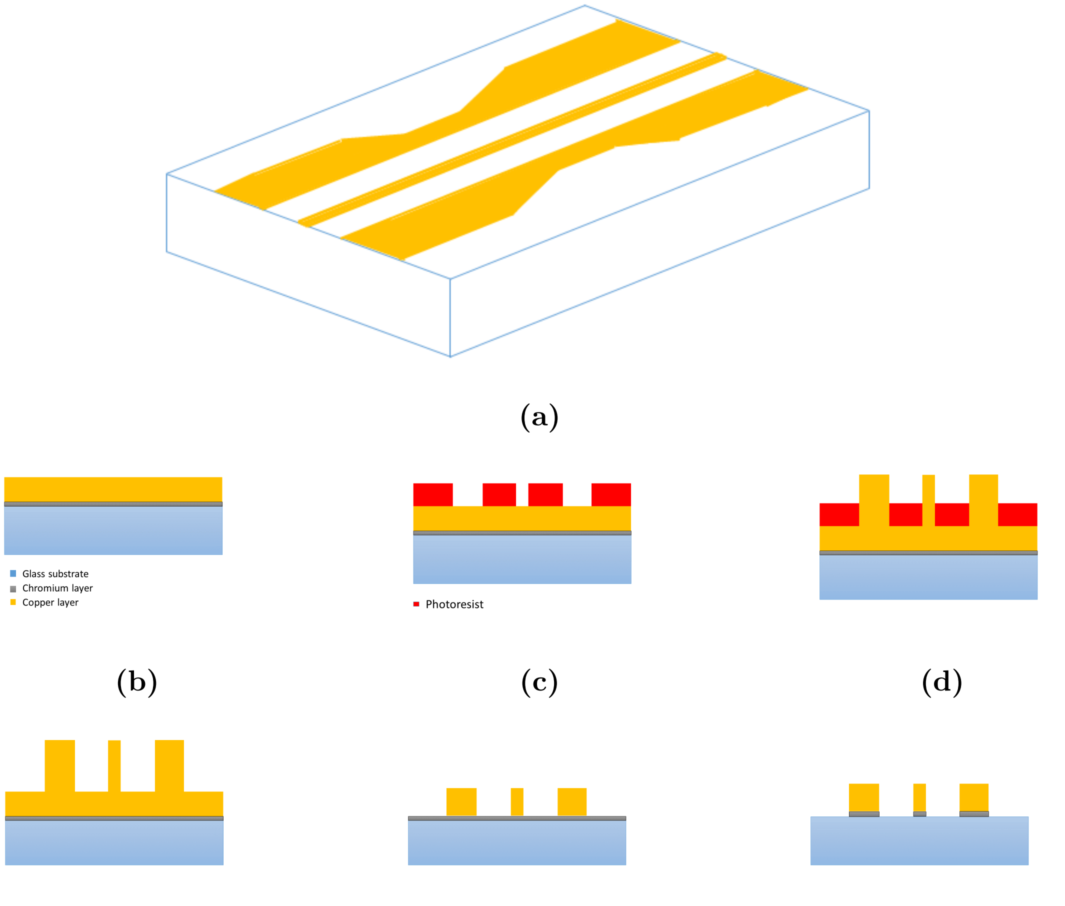

(a)

(b) (c) (d)

(e) (f) (g)

Figure 12: Planar waveguide fabrication process. (a) Planar waveguide fabricated on glass substrate. (b) Glass substrate having thin layers of chromium and copper. (c) A layer of photo resist was spin coated then exposed and developed to expose the area where we will do electroplating and grow a thicker copper layer of 20 µm. (d) A 20 µm layer of copper grown on the exposed area of copper seed. (e) Lift off: Removing the photo-resist. (f) Copper etching to remove the access copper from side areas. Some of the desired copper on the waveguide was removed as well. (g) Etching chromium.

4 Measurements and results

A nanodiamond dispersion purchased from (Adámas Nanotechnologies) having a concentration of 1 mg/mL, was diluted 50 times in water to reach a concentration of 20 µg/mL. The original dispersion of NDs is 40-45 nm in diameter, where each ND has 1-4 NVs. To ensure that after dilution we still have the same particle size and no aggregation has occurred, the new dispersion particle size was measured using Dynamic Light Scattering (DLS), Fig.13 shows the results, the average particle size is 55 nm, this value is higher than the size declared by the supplier, but should not change the results.

From the diluted dispersion, we drop cast on the co-planar waveguide fabricated in (section 3.2). For a better signal, we make sure that the drop is concentrated around the central line of the waveguide. We leave the waveguide in a fume hood for about an hour till the water evaporates. A very important phenomenon that we have seen during the evaporation that

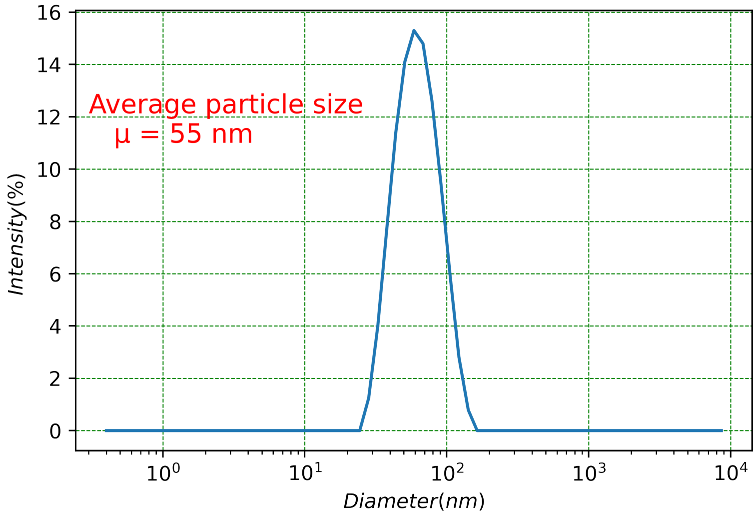

Figure 13: Dynamic Light Scattering (DLS) of the diluted NDs dispersion (20 µg/mL)

while the water evaporates the drop shrinks and its diameter becomes smaller, the NDs come closer to each other and form aggregates. This will raise the expected NV centers number in one confocal spot. After we make sure that all the water has evaporated, we place the waveguide in the confocal microscope (section 3.1.2) and connect it to the microwave system (section 3.1.3) from one side and terminate the other side of the WG with 50 Ω resistor to match the load and prevent undesired reflections.

Fig.14 shows a confocal scan of the NDs. Nearly every fluorescent spot in this confocal image is a cluster of NDs hosting NVs. Running ODMR as described in (section 2.4) on selected fluorescent points, we get spectra as shown in Fig. 15a. We fit the result with two Lorentzian functions, because a two level system emitting photons with no memory has an exponential decay, the Fourier transform (FT) of the exponential decay function is a Lorentzian function [27]. To calculate the axial and transverse strains, two parameters are required from this fit, shift and split. The split is calculated, at zero magnetic field (Appendix 6.4), as the distance between the two dips, and the shift is the displacement of the center point from the 2.87 GHz (ZFS) frequency from ODMR spctrum in Fig. 15a equals 11.35 ± 0.17 MHz, and 4.11 ± 0.17 respectively, linewidth of the Lorentzian, Γ, was 7.1 ± 0.16 MHz. This measurement was repeated on 247 different points from several confocal images, and both split and shift were extracted for each point. From the ODMR data collected for

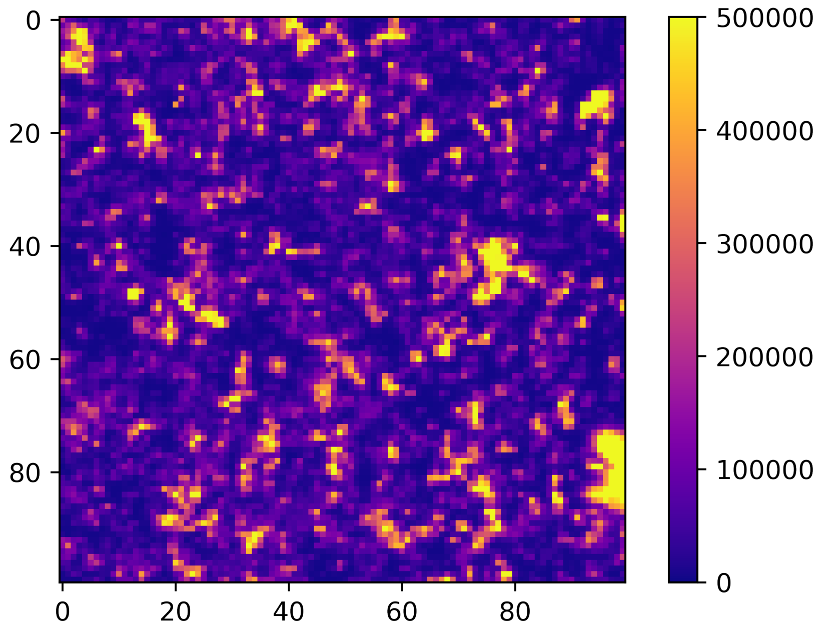

Figure 14: 80×80 µm confocal image of ND on glass substrate. Taken few microns from the central line of the waveguide. Most of the fluorescent points are ND aggregates

all the NDs, we plot a histogram for both split and shift Fig. 15b,c. The histograms were then fitted to Gaussian distribution. From the Gaussian fit, we extract the mean split and shift to be 11.35 ± 1.63 MHz and 4.43 ± 1.26 MHz respectively.

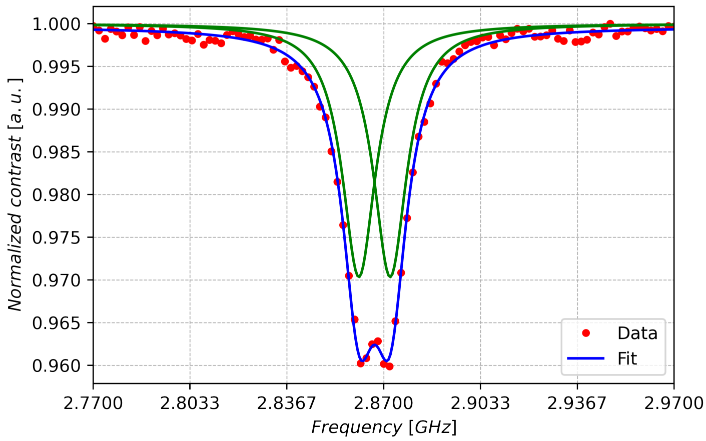

(a)

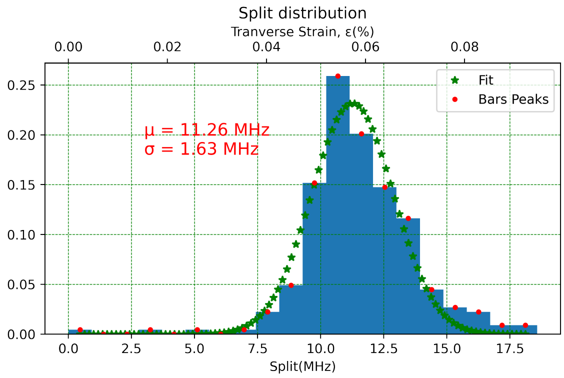

(b)

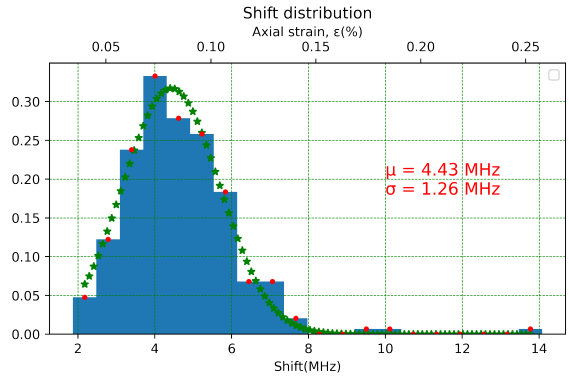

(c)

Figure 15: ODMR measurement of nanodiamonds containing NV centers. (a) ODMR of of one confocal spot showing both frequency split and shift, the blue curve is a Lorentzian fit of the two dips, the green curve shows each dips separate, and the red points are the measured data. (b) Histogram of the frequency split of 247 data points, the blue stars are Gaussian fit. c) Histogram of the shift of 247 data points the blue stars are Gaussian fit.

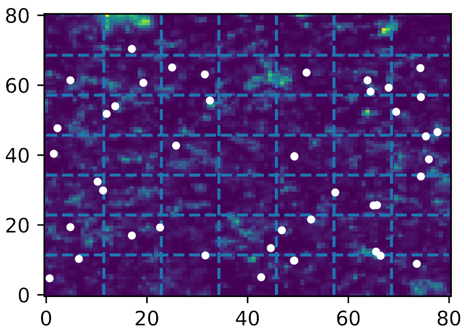

(a)

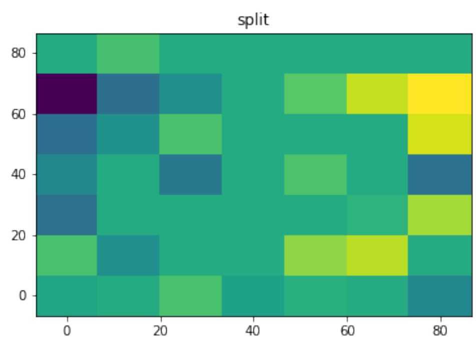

(b)

Figure 16: Code image (a) Confocal image of 44 NDs, the white spots mark the positions of the clusters of NDs on which we measured ODMR. (b) Color code image reflecting frequency split. Squares that do not contain NDs are set to the mean value.

5 Discussion and Conclusion

In recent years, many studies were performed on NV centers, investigating different aspects of them. Mainly because of their potential to be used as qubits. Other studies considered strain in bulk diamond. To the best of our knowledge, there are no studies considering strain in NDs. In this study we were able to characterize strain in a cluster of FNDs, and see that every cluster has its unique strain. We also believe that the distribution of FNDs clusters strain is correlated to the particle size, and future studies will be needed to confirm this hypothesis.

Each cluster of FNDs has its unique axial and transverse strain values, corresponding to a unique frequency split and shift in their ODMR spectra. This can be exploited in two ways, the first is time tracking of a specific FND, a good example for this is bio-markers in living cells where the purpose is to monitor and time trace cell parameters such as temperature and pH. This type of tracing will give us, with high confidence the sensors' identity and position. The second is unclonable anti-counterfeiting labels. For this application we scanned an $80 \times 80\,\mu\text{m}^2$ confocal image Fig16a, here we have 44 FNDs, each shown as a white spot. We divide this image into 7×7 squares and plot a representative color map of the axial strain (Fig. 16b) . The same can be done with the transverse strain, squares that do not contain FNDs are set to the average strain value for reasons of color offsetting. This color map can be used as a color code of the strain values of the confocal image. Different types of encoding the strain data may be used, such as QR-code. As QR-codes are becoming more popular and are a part of every smartphone, we also suggest to encode the data using QR-code. In this technique we encoded four different parameters of each FND (x, y, split, and shift), see Fig.18.

Due to technical restrictions, we could not get single particles dispersed on the glass substrate. We tried three different methods to achieve single particles dispersed on the substrate, and each time we tested this by running $g^{(2)}$ auto-correlation test [28]. The first method was drop casting, which is the one we used for this study. The problem in this method is that we could not achieve single particle FNDs dispersed on the glass substrate, and we only got aggregates of about 40 particles. We think this is due to the relative slow water evaporation of the drop - this evaporation causes shrinking of the drop from the sides, which results in FND particles from the sides diffusing to the center, and coming closer to each other and aggregate. The second method was spin coating. We tried different spin coating parameters, to get single particles dispersed on the substrate. In this method, too, we did not succeed to achieve single NDs on the substrate. The third method arose from the fact that it takes long time for water to evaporate, and it has a relatively bad wetting angle with the glass substrate. For this we chose methanol as an alternative to water, where it evaporates faster and has a better wetting angle, giving it a better spread on the substrate. The problem in this method is that no NDs were found on the substrate after evaporation, where we believe they were bonded to methanol in the evaporation process, leaving no FNDs on the substrate. To get a trade-off between the two mechanisms, aggregation, and complete evaporation, and overcome this obstacle we used a water:methanol solution of different percentages to get the right balance between the two mechanisms. Also here we could not achieve single NDs dispersed on the substrate, where in high water concentrations we got aggregates of FNDs, and in high methanol concentrations we saw nothing, and no optimal point was found. Further research to find an optimal point may be conducted.

The method we used to prepare the samples is good for lab-experimental purposes, but to have a low cost massive production method, we suggest that small chips (starting by big wafers), then, disperse the FNDs by printing [29] them on a substrate having a co-waveguide patterned on it, or CVD growth [30] in a controllable manner of the size and numbers of

NVs on a wafers as mentioned before. More research needs to be done to show the feasibility of the suggested methods to fabricate code-chips containing FNDs.

As we mentioned before, we were not able to separate single FNDs. From SEM images we estimate the number of FNDs in a cluster to be nearly n=40. Nine ODMR spectra of nine different clusters of FNDs are shown in Fig. 20. To check the consistency of our calculations, we simulated the ODMR spectrum of 40 FNDs, drawing their sum, where the split and shift values were drawn from the normal distribution Fig. 15b,c. Fig. 17a which shows that even for a large cluster of NVs (n=40) we get a distinct ODMR spectra. This leads us to figure out a way to quantify the fidelity of our measurement to distinguish between two neighboring dips, Fig. 17b, we chose four different acquisition times (2500, 250, 100 and 25 seconds), each curve shows a different acquisition time. For example lets take T=2500 s, for this acquisition time the noise $\gamma = 0.12$ MHz, we chose randomly two different dips from the normal distribution Fig. 15c, then, we calculated the difference between them, $\Delta\omega = |\omega_1 - \omega_2|$, we compare each time this difference to the relative noise of the acquisition time, whenever $\Delta\omega > \gamma$, we mark this as distinguishable dips, then, we sum the times we succeeded to distinguish two dips out of 1000 trials, for each possible normal distribution marked on the x-axis. Here, assume we want 80% fidelity threshold (horizontal dashed line), for a given normal distribution having $\sigma = 1.25$ MHz or larger, an acquisition time between T=250 s and T=100 s, will be sufficient.

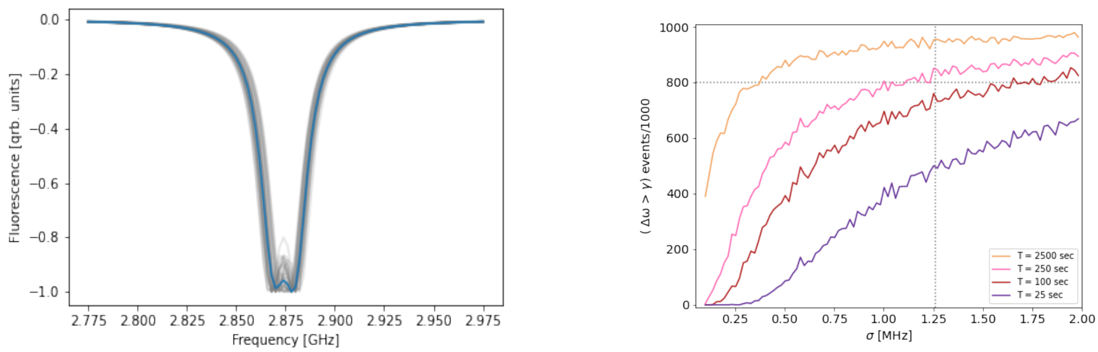

(a) (b)

Figure 17: (a) Simulation showing the sum of 40 NVs ODMR spectra (b) Quantifying the ability to distinguish between two neighboring nanodiamond clusters. Each curve represents different acquisition time (2500, 250, 100 and 25 seconds), the x-axis is the standard deviation of the relative Gaussian distribution and the y-axis is the number of times per thousand we succeed to distinguish between two neighboring dips for the given standard deviation. The dashed lines are one example of the measure of fidelity for $\sigma = 1.25$ MHz, and certainty above 80%.

Figure 18: QR-code representing xy coordinates, axial, and transverse strain of 247 FNDs.

When the transverse strain is too small, then the split will be accordingly small, if the linewidth of each dip is big enough then the dips will overlap showing one dip only. The average linewidth of the Lorentzian in the ODMR spectra was nearly 7 MHz. To check a criterion of when we can visually distinguish between two different dips, I simulated several ODMR spectra with different split values. Fig. 19 shows that the criterion is satisfied when the split is bigger than half the linewidth.

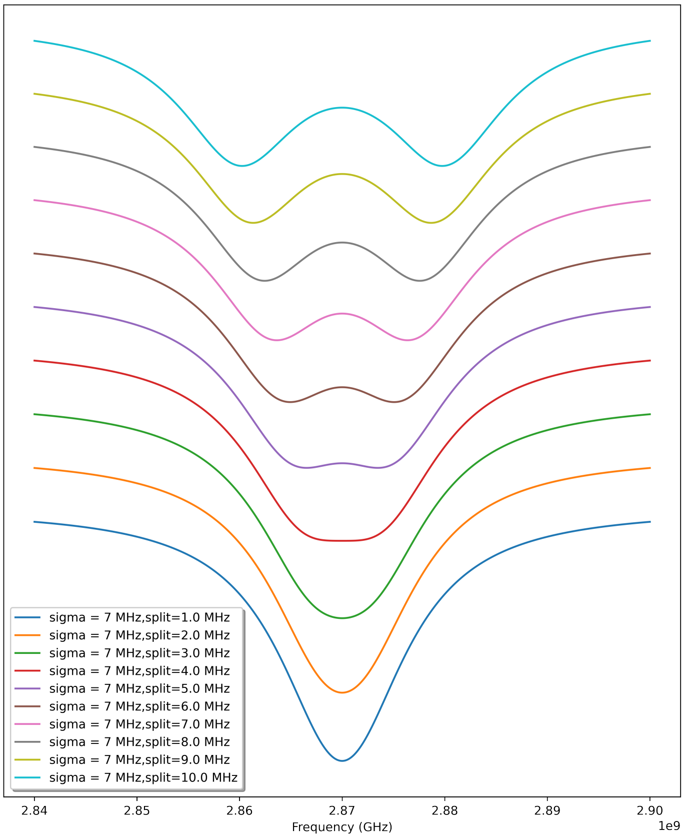

Figure 19: ODMR spectra: each curve shows different split with line width 7 MHz, the two dips are visually observed when the split is more than 4 MHz.

6 Appendices

6.1 Microwave

To fully understand the IQ mixers function and its ability to scan over a range of frequencies, recall the following trigonometric identities, in these identities for simplicity we drop the $2\pi t$ terms.

$$\cos{(f-\frac{\pi}{2})} = \sin(f) \tag{6.1}$$

$$\cos{(f+\frac{\pi}{2})} = -\sin(f) \tag{6.2}$$

$$\cos\alpha\cos\beta = \frac{1}{2}[\cos{(\alpha+\beta)} + \cos{(\alpha-\beta)}] \tag{6.3}$$

$$\sin\alpha\sin\beta = \frac{1}{2}[\cos{(\alpha-\beta)} - \cos{(\alpha+\beta)}] \tag{6.4}$$

here we assume that the default signal is $cos(f)$, so if both the oscillator and mixing signal are in phase we get two harmonics, one with frequency of the sum $f_c + f_w$ and the other with the difference frequency $f_c - f_w$

$$\cos f_c \times \cos f_w = \frac{1}{2}[\cos{(f_c+f_w)} + \cos{(f_c-f_w)}] \tag{6.5}$$

and if both are $-\frac{\pi}{2}$ phase shift,

$$\begin{aligned}\cos{(f_c-\frac{\pi}{2})} \times \cos{(f_w-\frac{\pi}{2})} &= \sin f_c \times \sin f_w \\ &= \frac{1}{2}[\cos{(f_c-f_w)} - \cos{(f_c+f_w)}]\end{aligned} \tag{6.6}$$

but if the phase shift is $+\frac{\pi}{2}$ we get,

$$\begin{aligned}\cos{(f_c-\frac{\pi}{2})} \times \cos{(f_w+\frac{\pi}{2})} &= \sin f_c \times (-\sin f_w) \\ &= \frac{1}{2}[\cos{(f_c+f_w)} - \cos{(f_c-f_w)}]\end{aligned} \tag{6.7}$$

to scan over the right side of the center frequency(lower frequencies than center frequency), both the in phase (eq 6.5) and $-\frac{\pi}{2}$ phase shift (eq6.6) are fed to an adder and get the right side frequency $f_c - f_w$

$$\begin{aligned}&\cos f_c \times \cos f_w + \cos{(f_c-\frac{\pi}{2})} \times \cos{(f_w-\frac{\pi}{2})} \\ &= \frac{1}{2}[\cos{(f_c+f_w)} + \cos{(f_c-f_w)}] + \frac{1}{2}[\cos{(f_c-f_w)} - \cos{(f_c+f_w)}] \\ &= \cos{(f_c-f_w)}\end{aligned} \tag{6.8}$$

to scan for the left hand side frequencies (frequencies lower than the center frequency), we apply $+\frac{\pi}{2}$ phase shift to the quadrature part of the signal(eq6.7), and we get

$$\begin{aligned}&\cos f_c \times \cos f_w + \cos{(f_c-\frac{\pi}{2})} \times \cos{(f_w+\frac{\pi}{2})} \\ &= \frac{1}{2}[\cos{(f_c+f_w)} + \cos{(f_c-f_w)}] + \frac{1}{2}[\cos{(f_c+f_w)} - \cos{(f_c-f_w)}] \\ &= \cos{(f_c+f_w)}\end{aligned} \tag{6.9}$$

so for example as we saw in the ODMR, let's assume that the center frequency is 2.87 GHz which is the zero field splitting, and we want to scan over five different frequencies $[2.85, 2.86, 2.87, 2.88, 2.89]$ (GHz) so our intermediate frequencies will be $[20, 10, 0, 10, 20]$ (MHz), with the right phase shift as mentioned above.

6.2 Electroplating

To derive a formula for thickness, current, and process time, remembering that copper has an fcc structure with lattice parameter $a = 0.3615$ nm, in fcc structure we have 4 atoms per unit cell.
The time needed to deposit one mole of copper is $t = \frac{n_e \times e_c \times N_v}{I}$ where n_e is the number of electron needed for one copper atom to be reduced to the zero valence state and equal to 2 for Cu^{2+}, e_c is the electron charge, and N_v is Avogadro's number. Number of atoms per one copper layer $N_t = \frac{A_s}{a^2} \times 4$ and so number of moles per layer will be $N_m = \frac{N_t}{N_v}$ where N_v is Avogadro's number. From this we get the time for one layer deposition $t_l = t \times N_m$ one layer will have the height of (a) which is the lattice parameter and generally for any thickness we get,

$$\begin{aligned} \frac{t_{total}(\mathrm{s})}{h(\mathrm{m})} &= \frac{t \times N_m}{a} \\ &= \frac{n_e \times e_c \times N_v \times A_s \times 4}{I \times N_v \times a^3} \end{aligned} \tag{6.10}$$

using the formula for current density $J = I/A$

$$\frac{t_{total}(\mathrm{s})}{h(\mathrm{m})} = \frac{1}{J} \times \frac{n_e \times e_c \times n_{lattice}}{a^3} \tag{6.11}$$

define the constant $C = \frac{n_e \times e_c \times n_{lattice}}{a^3}$,
for copper it will be equal to $C = \frac{2 \times 1.6 \times 10^{-19} \times 4}{(0.3615 \times 10^{-9})^3} = 271 \times 10^8 \, \mathrm{C/m^3}$
the whole equation can be rewritten while h(µm) and I($\mathrm{mA/cm^2}$) and t(minutes)

$$\frac{t_{total}}{h(\mu\mathrm{m})} = \frac{45.16}{J} \tag{6.12}$$

6.3 3×3 matrix code

Different approaches and code designs can be made using FNDs, the color code or QR-code are one example. Here we show another possibility of using 3×3 matrix of 9 FNDs ODMR spectra.

6.4 Shielding the NV center from external magnetic fields

Earth has a magnetic field of about 0.5 Gauss. Other magnetic noise sources may come from different equipment in the lab. To verify that what we are measuring is strain field only, we purchased from Magnetic Shields Limited [31] a magnetic shield box made out of mu-metal magnetic shielding material. This box shields the NV centers from external magnetic fields. The NV center is thus fully protected, except for a small opening from the objective side to scan the sample.

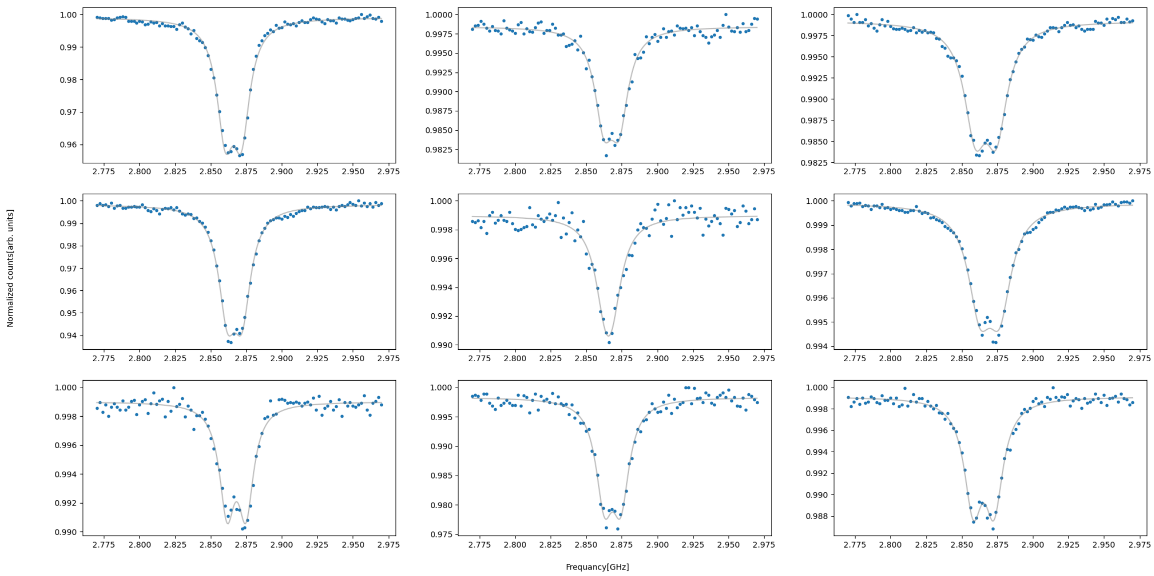

Figure 20: A 3×3 ODMR spectra of 9 FNDs arranged in a square matrix

To verify that there are no magnetic fields affecting our strain measurement, we performed ODMR measurement, with the shielding box, and without the shielding box. Both measurements were identical, showing that there are no magnetic fields interfering with the strain field, and the measurement does not have a magnetic field effect.

References

[1] Vadym N Mochalin, Olga Shenderova, Dean Ho, and Yury Gogotsi. The properties and applications of nanodiamonds. *Nature nanotechnology*, 7(1):11–23, 2012.

[2] KiranJ van der Laan, Masoumeh Hasani, Tingting Zheng, and Romana Schirhagl. Nanodiamonds for in vivo applications. *Small*, 14(19):1703838, 2018.

[3] Cécile Vincent, Jean-François Silvain, Jean-Marc Heintz, and Namas Chandra. Effect of porosity on the thermal conductivity of copper processed by powder metallurgy. *Journal of Physics and Chemistry of Solids*, 73(3):499–504, 2012.

[4] FM Stürner, Y Liu, P-O Colard, M Markham, and F Jelezko. Magnetometry based on the excited-state lifetimes of a single nitrogen-vacancy center in diamond. *Applied Physics Letters*, 119(13):134001, 2021.

[5] William Henry Bragg and William Lawrence Bragg. The structure of the diamond. *Proceedings of the Royal Society of London. Series A, Containing Papers of a Mathematical and Physical Character*, 89(610):277–291, 1913.

[6] Marcus W Doherty, Neil B Manson, Paul Delaney, Fedor Jelezko, Jörg Wrachtrup, and Lloyd CL Hollenberg. The nitrogen-vacancy colour centre in diamond. *Physics Reports*, 528(1):1–45, 2013.

[7] J Meijer, B Burchard, M Domhan, C Wittmann, Torsten Gaebel, I Popa, F Jelezko, and J Wrachtrup. Generation of single color centers by focused nitrogen implantation. *Applied Physics Letters*, 87(26):261909, 2005.

[8] II Vlasov, Victor G Ralchenko, AV Khomich, SV Nistor, D Shoemaker, and RA Khmelnitskii. Relative abundance of single and vacancy-bonded substitutional nitrogen in cvd diamond. *physica status solidi (a)*, 181(1):83–90, 2000.

[9] Linh My Pham, N Bar-Gill, D Le Sage, C Belthangady, A Stacey, M Markham, DJ Twitchen, Mikhail D Lukin, and Ronald L Walsworth. Enhanced metrology using preferential orientation of nitrogen-vacancy centers in diamond. *Physical Review B*, 86(12):121202, 2012.

[10] Srujan Meesala, Young-Ik Sohn, Haig A Atikian, Samuel Kim, Michael J Burek, Jennifer T Choy, and Marko Lončar. Enhanced strain coupling of nitrogen-vacancy spins to nanoscale diamond cantilevers. *Physical Review Applied*, 5(3):034010, 2016.

[11] J Teissier, A Barfuss, P Appel, E Neu, and P Maletinsky. Strain coupling of a nitrogen-vacancy center spin to a diamond mechanical oscillator. *Physical review letters*, 113(2):020503, 2014.

[12] Preeti Ovartchaiyapong, Kenneth W Lee, Bryan A Myers, and Ania C Bleszynski Jayich. Dynamic strain-mediated coupling of a single diamond spin to a mechanical resonator. *Nature communications*, 5(1):1–6, 2014.

[13] JP Tetienne, L Rondin, P Spinicelli, M Chipaux, T Debuisschert, JF Roch, and V Jacques. Magnetic-field-dependent photodynamics of single nv defects in diamond: an application to qualitative all-optical magnetic imaging. *New Journal of Physics*, 14(10):103033, 2012.

[14] N. B. Manson, J. P. Harrison, and M. J. Sellars. Nitrogen-vacancy center in diamond: Model of the electronic structure and associated dynamics. *Phys. Rev. B*, 74:104303, Sep 2006.

[15] Fedor Jelezko and Jörg Wrachtrup. Single defect centres in diamond: A review. *physica status solidi (a)*, 203(13):3207–3225, 2006.

[16] A Dréau, M Lesik, L Rondin, P Spinicelli, O Arcizet, J-F Roch, and V Jacques. Avoiding power broadening in optically detected magnetic resonance of single nv defects for enhanced dc magnetic field sensitivity. *Physical Review B*, 84(19):195204, 2011.

[17] V Blank and M Popv. G. pivovarov, n. lvova, k. gogolinsky, v. reshetov. *Diamond and Related Materials*, 7:427, 1998.

[18] HP Bovenkerk, FP Bundy, RM Chrenko, PJ Codella, HM Strong, and RH WentorfJr. Errors in diamond synthesis. *Nature*, 365(6441):19–19, 1993.

[19] KV Volkov, VV Danilenko, and VI Elin. Synthesis of diamond from the carbon in the detonation products of explosives. *Combustion, Explosion and shock waves*, 26(3):366–368, 1990.

[20] Olga A Shenderova and Suzanne A Ciftan Hens. Detonation nanodiamond particles processing, modification and bioapplications. In *Nanodiamonds*, pages 79–116. Springer, 2010.

[21] Jean-Paul Boudou, Patrick A Curmi, Fedor Jelezko, Joerg Wrachtrup, Pascal Aubert, Mohamed Sennour, Gopalakrischnan Balasubramanian, Rolf Reuter, Alain Thorel, and Eric Gaffet. High yield fabrication of fluorescent nanodiamonds. *Nanotechnology*, 20(23):235602, 2009.

[22] James E Butler and Henry Windischmann. Developments in cvd-diamond synthesis during the past decade. *MRS Bulletin*, 23(9):22–27, 1998.

[23] Walter A Yarbrough and Russell Messier. Current issues and problems in the chemical vapor deposition of diamond. *Science*, 247(4943):688–696, 1990.

[24] Guo-Wei Yang, Jin-Bin Wang, and Qui-Xiang Liu. Preparation of nano-crystalline diamonds using pulsed laser induced reactive quenching. *Journal of Physics: Condensed Matter*, 10(35):7923, 1998.

[25] Jan M Binder, Alexander Stark, Nikolas Tomek, Jochen Scheuer, Florian Frank, Kay D Jahnke, Christoph Müller, Simon Schmitt, Mathias H Metsch, Thomas Unden, et al. Qudi: A modular python suite for experiment control and data processing. *SoftwareX*, 6:85–90, 2017.

[26] Thorlabs Inc. `https://www.thorlabs.com`. Accessed: 2022-11-30.

[27] A Dréau, M Lesik, L Rondin, P Spinicelli, O Arcizet, J-F Roch, and V Jacques. Avoiding power broadening in optically detected magnetic resonance of single nv defects for enhanced dc magnetic field sensitivity. *Physical Review B*, 84(19):195204, 2011.

[28] Janik Wolters, Andreas W Schell, Günter Kewes, Nils Nüsse, Max Schoengen, Henning Döscher, Thomas Hannappel, Bernd Löchel, Michael Barth, and Oliver Benson. Enhancement of the zero phonon line emission from a single nitrogen vacancy center in a nanodiamond via coupling to a photonic crystal cavity. *Applied Physics Letters*, 97(14):141108, 2010.

[29] Zhaoyi Xu, Lingzhi Wang, Xiao Huan, Heekwon Lee, Jihyuk Yang, Zhiwen Zhou, Mojun Chen, Shiqi Hu, Yu Liu, Shien-Ping Feng, et al. On-demand, direct printing of nanodiamonds at the quantum level. *Advanced Science*, 9(5):2103598, 2022.

[30] James E Butler and Anirudha V Sumant. The cvd of nanodiamond materials. *Chemical Vapor Deposition*, 14(7-8):145–160, 2008.

[31] Magnetic Shields Limited. `https://magneticshields.co.uk/`. Accessed: 2022-11-30.

7 Acknowledgement

At the end I would like to thank all the people who helped me to accomplish this research, starting by my advisor Dr. Amit Finkler, for letting me be part of his group, which gave me a great opportunity to learn new things, and for his patience and continuous availability. Also I would like to thank Inbar Zohar for training, and guiding me through all my way specially on using the setup, that was built by her (Beyonce). Finally, I would thank all my colleagues, Ariel Smooha, Dan Yudilevich, Dr. Jitender Kumar, Leora Schein-Lubomirsky, and John Woodrow Rosenberg for the fruitful discussions, and explanation. It is a great opportunity to work with you all.

Working on this project introduced me to a new field, and enhanced my scientific research tools, giving me the feeling of satisfaction. All this would not happen without the help of my advisor and colleagues, so, thank you all again.